PHYSICS OF ELEMENTARY PARTICLES
AND ATOMIC NUCLEI. EXPERIMENT

DANSS Neutrino Spectrometer: Detector Calibration, Response Stability, and Light Yield

I. G. Alekseev[a, b, c], V. V. Belov[d], M. V. Danilov[b, c, e], I. V. Zhitnikov[d, *], A. S. Kobyakin[a, b],
A. S. Kuznetsov[d], I. V. Machikhiliyan[a, b, **], D. V. Medvedev[d], V. Yu. Rusinov[a],
D. N. Svirida[a, b], N. A. Skrobova[a, b, e], A. S. Starostin[a, b], E. I. Tarkovsky[a], M. V. Fomina[d],
E. A. Shevchik[d], and M. V. Shirchenko[d]

[a]*Alikhanov Institute for Theoretical and Experimental Physics, Moscow, 117218 Russia*
[b]*Moscow Institute of Physics and Technology (State University), Dolgoprudnyi, Moscow oblast, 141700 Russia*
[c]*National Research Nuclear University MEPhI, Moscow, 115409 Russia*
[d]*Joint Institute for Nuclear Research, Dubna, Moscow oblast, 141980 Russia*
[e]*Lebedev Physical Institute, Russian Academy of Sciences, Moscow, 119991 Russia*
*e-mail: i.zhitnikov@gmail.com
**e-mail: machikhiliyan@itep.ru
Received November 14, 2017

Abstract—Apart from monitoring nuclear reactor parameters, the DANSS neutrino experiment is aimed at searching for sterile neutrinos through a detailed analysis of the ratio of reactor antineutrino spectra measured at different distances from the reactor core. The light collection system of the detector is dual, comprising both the vacuum photomultiplier tubes (PMTs) and silicon photomultipliers (SiPMs). In this paper, the techniques developed to calibrate the responses of these photodetectors are discussed in detail. The long-term stability of the key parameters of the detector and their dependences on the ambient temperature are investigated. The results of detector light yield measurements, performed independently with PMTs and SiPMs are reported.

1. THE DANSS EXPERIMENT

The DANSS compact neutrino spectrometer [1] is located beneath the core of one of industrial reactors of the Kalinin nuclear power plant. Reactor antineutrinos are detected by selecting and reconstructing the events of inverse β-decay, $\overline{\nu}_e + p \rightarrow e^+ + n$. In contrast with previous similar experiments, the sensitive volume of the detector is made of a plastic scintillator with no flammable and toxic materials. This enabled us to install the detector only a few meters from the center of the reactor core, taking full advantage of the high antineutrino flux at this location.

The detector body is a cube built of 1-m-long scintillator slabs (or strips) with a cross section of 4×1 cm^2. Each slab is coated with a material which contains gadolinium as a substance with a large cross section for the radiative capture of thermal neutrons. Each detector layer consists of 25 scintillator strips and is rotated by 90° with respect to the lower one, as is shown in Fig. 1a. The rigidity of the structure is provided by copper frames, each supporting two planes of mutually orthogonal strips. Twenty successive layers form a section as a basic structural unit of the setup. The detector as a whole consists of five vertically mounted sections and also includes the top and bottom copper plates. The total sensitive volume of the detector amounts to 1 m^3.

Owing to its location, the detector is adequately shielded from downward cosmic rays by a large volume of concrete, the reactor body, and the tanks containing technological liquids. The resultant overburden of 50 m.w.e. practically eliminates the fast-neutron background from distant sources and reduces the muon background by a factor of nearly six. The detector is additionally enclosed in a multilayer passive and active shielding, whose composition is shown in Fig. 1b. The backgrounds arising from gamma rays and thermal and epithermal neutrons are suppressed by the passive shielding, which is formed by the copper frames of the detector (with a thickness of 5 cm), an inner screen of borated polyethylene (8 cm), a lead layer (5 cm), and an outer screen of borated polyethylene (8 cm). The active shielding is formed by two layers of rectangular scintillator slabs placed on top of the outer screen and covering the upper and lateral facets of the cube (32 slabs). The dead areas at the lateral edges of the cube are additionally shielded with eight scintillation counters. This veto system is aimed at further suppression of the muon component of the cosmic background.
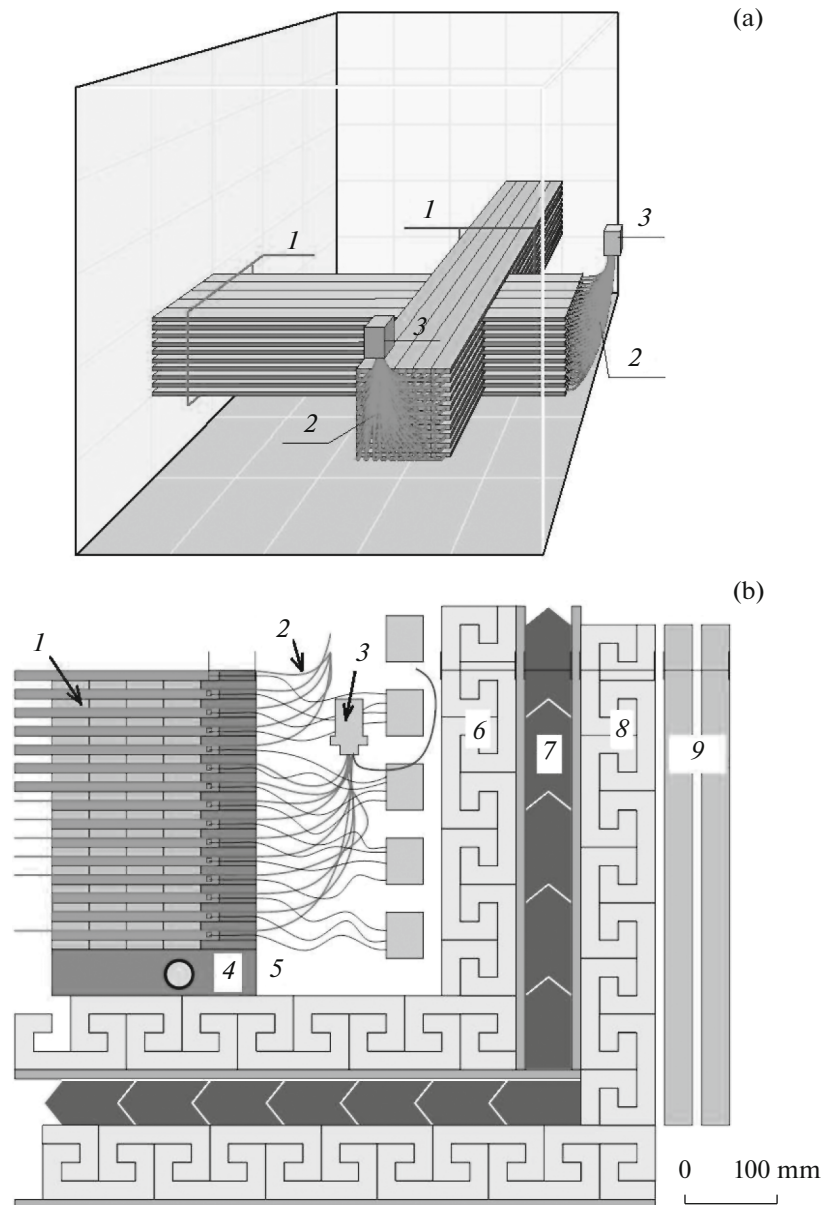
Fig. 1. Panel (a): scheme of the detector layout showing the strips forming a module (*1*), light-shifting fibers (*2*), and a photomultiplier tube (*3*). Panel (b): structure of the shielding showing the sensitive volume (*1*), wavelength shifting fibers (*2*), a photomultiplier tube (*3*), copper frames (*4*), the gap housing the photodetectors (*5*), the inner borated polyethylene screen (*6*), the lead layer (*7*), the outer borated polyethylene screen (*8*), and veto counters (*9*).

The whole detector is mounted on an elevator platform, whereby its distance from the reactor core can be varied. The detector position is changed after every 2–3 days of operation in order to reduce the systematic errors. The data are collected at the top, medium, and bottom detector positions corresponding to distances of 10.7, 11.7, and 12.7 m from the center of the reactor core. It provides an excellent opportunity to search for the neutrino transition to a hypothetic sterile state over a broad range of mixing parameters values. The detector position is measured automatically and recorded together with the experimental data. No data are logged while the detector is moved from one position to another.

The trigger on the events of inverse β-decay is issued as soon as the net prompt energy release exceeds the threshold value of 0.7 MeV. Additionally, all events with an activity in the veto system are logged on disk. The data are collected at an overall frequency of 1 kHz and saved to uniquely numbered computer files. In the normal regime, each file contains about 1.5 million events collected in 25–30 min of detector operation. With this rate of data collection, nearly 5000 inverse-β-decay events can be reconstructed per day of detector operation in the position closest to the reactor core. The residual contribution of cosmic background in the sample is less than 1%.
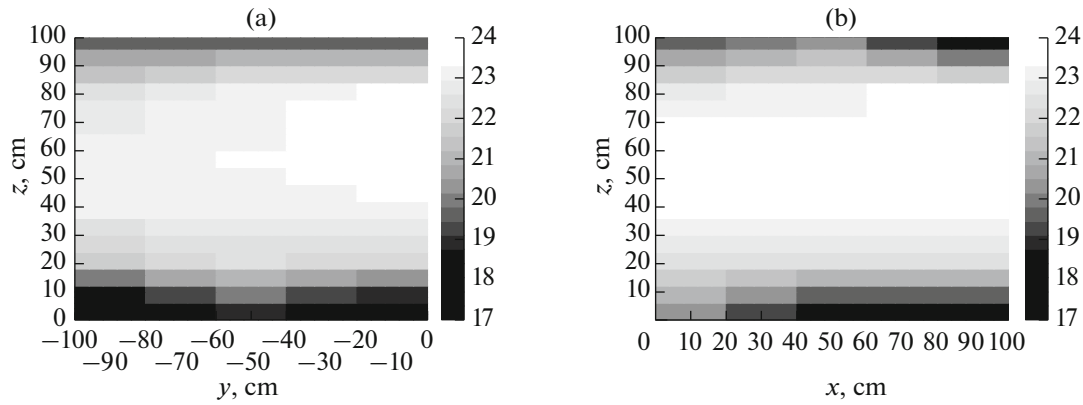
Fig. 2. Typical temperature maps of the readout planes.

2. SYSTEMS OF LIGHT COLLECTION AND PHOTODETECTION

From each scintillator strip, light is collected using three Y11 wavelength shifting optical fibers with a 1.2-mm diameter manufactured by Kuraray. These are glued into 2.5-mm-deep grooves running along the strip face at equal distances from each other and from the longitudinal edge facets. The fibers are read out by photodetectors of two types mounted on neighboring side facets of the detector cube: the silicon photomultipliers (SiPMs) and ordinary vacuum photomultiplier tubes (PMTs). For every 50 strips with the same orientation forming a five-strip-wide part of a section, the pairs of noncentral fibers are bundled together (see Fig. 1a), delivering light to a PMT photocathode. Through the central fibers, the strips are read out individually using SiPMs. In what follows, the readout edge of a strip is referred to as a detector cell, and a group of 50 cells read out by a single PMT is referred to as a module. The module size has been chosen taking into account the spatial characteristics of typical DANSS neutrino events, which are restricted to spherical areas with radii of some 30 cm.

The implementation of a dual light collection system is motivated by the following arguments. Given the fine segmentation of the detector and a restricted space available for placing the photodetectors, small-size and low-cost SiPMs are best suited for individual readout of each cell. The latter is required for obtaining a detailed space–energy pattern of an event as one of the key factors in reconstructing the events of inverse β-decays. However, relying on SiPMs for forming a fast and reliable trigger signal is complicated by their drawbacks: the irreducible low-amplitude dark noise and temperature dependence of their parameters. Therefore, the detector triggering system is based on traditional photomultiplier tubes, which are affected less by external conditions and provide a more accurate estimate of the total energy release, albeit with an inferior spatial resolution due to the relatively large module size. At the same time, the accumulated data are analyzed using both the PMT and SiPM signals. This enables us to fully exploit the advantages of both types of photodetectors and carry out various cross checks towards measuring the reactor antineutrino spectra to better precision and quality.

In the veto system, light is collected from the two longitudinal side facets of a scintillator slab. The corresponding optical wavelength shifting fibers are read out by a vacuum PMT at one of the counter edges.

In total, the DANSS detector employs 2500 SiPMs, 50 PMTs for reading out the modules, and 40 PMTs of the veto system. All photodetectors were manufactured by Hamamatsu Photonics. The compact PMTs are of the R7600U-300 type with a photocathode effective area of 18×18 mm^2, and the SiPMs are of the MPPC S12825-050C type with a sensitive area of 1.3×1.3 mm^2 containing 667 pixels. The veto system relies on the H10720-20 photodetector modules.

With the exception of the veto system, the photodetectors and the readout electronics reside in the gap between the copper frames and the inner borated polyethylene screen forming two readout planes. Each plane serves 1250 cells and 25 modules.

Since the heat dissipation is strongly impeded by the passive shielding, the detector is additionally cooled with water which is pumped through pipes inserted in the aforementioned gap. The readout planes are instrumented with 36 temperature sensors uniformly distributed over both facets of the cube. These are read out every 5 min using the monitoring software, whereby the temperature at SiPM positions is measured. Typical temperature maps of the two planes are shown in Fig. 2, where interpolation was performed in the intersensor areas. The temperature gradients are largely determined by the arrangement of the cooling pipes. The temperature varies between 17 and 24°C.

Apart from the cooling system pipes, the gap houses 50 optical fibers used for delivering the light of an external LED to the PMT photocathodes. The

LED light is injected solely during the test runs which are conducted to study the characteristics of the PMTs (see Section 8).

3. DIGITIZATION OF PHOTODETECTOR SIGNALS

The photodetectors are read out by a system of 64-channel UWFD64 modules developed for the DANSS experiment at the Alikhanov Institute for Theoretical and Experimental Physics (Moscow). Their tasks include forming the signals, compensating for the baseline shift, digitizing signals with 12-bit analog-to-digital converters (ADCs), buffering the data, and issuing the trigger signal. The SiPM system is served by 44 modules, and two additional modules are reserved for reading out the detector and veto-system PMTs, respectively.

Data acquisition (DAQ) in the DANSS experiment is specific in that the response of an individual channel is recorded as a signal time profile digitized with an 8-ns step in a 512-ns time window rather than as a single ADC signal. This window is formed around the signal pulse maximum upon triggering on a given event. A typical time profile of SiPm signal is exemplified in Fig. 3. For a small fraction of events, the shape of the time profile can be distorted by the SiPM noise or by parasitic pulses from physical particles that may randomly fall within the time window. The preprocessing software allows one to identify the signal pulse and estimate its parameters (of these, the most important ones are the signal arrival time t_0 and the integral I normalized to the 8-ns width of the time bin). The value of I is a measure of energy release in a cell, module, or veto counter. An additional signal selection according to the value of t_0 helps suppress the random pulses when reconstructing the parameters of secondary particles in inverse β-decay.

4. CALIBRATION PROCEDURE

Energy calibration is aimed at establishing a relation between the integral signal I obtained by preprocessing the signal time profile and the actual energy release in a given detector cell, detector module, or veto counter. The digitized response of the system to a particle passing through the detector is determined by multiple factors, including the efficiencies of deposited energy conversion to scintillation photons and of their capture by the wavelength shifting fiber, the light pulse attenuation as it is transported to the sensitive area of a photodetector, the latter's characteristics in transforming light into an electric current, and the properties of the DAQ analog–digital tract. The scintillator and optical fiber properties remain stable, albeit they may differ for different channels of the detector. In contrast, the photodetector characteristics can be strongly affected by factors such as external
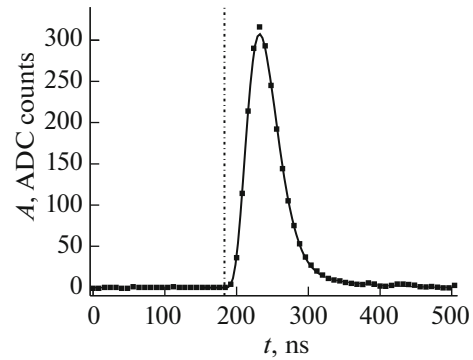

Fig. 3. Typical pulse shape of a SiPM signal. The vertical line marks the signal arrival time t_0.

conditions, operational settings, and duration of continuous illumination.

Our experience with running DANSS for over a year suggests that, of all external factors, detector stability is most strongly affected by variations of temperature T. Though the passive shielding acts as a thermostat, residual T variations are always detected in the gap housing the photodetectors (arising from, e.g., changing the detector position). The time variation of the mean temperature of readout planes over a long period of continuous data taking between May 17 and July 9, 2017, is shown in Fig. 4, together with that of the detector position (dashed line). The heating of readout planes is seen to be stronger the higher the detector position is. That the temperature tends to slowly increase with time is probably due to the seasonal warming of the experimental hall.

All this poses an important problem of developing a reliable procedure for calibration of each detector channel at least once every 2–3 days. This is particularly important for SiPMs, due to nonlinear dependence of their signal on the number of detected photons and temperature instability of their parameters. Apart from that, the responses of silicon photomultipliers can be affected by the possible T-dependence of the output voltages provided by the SiPM power-supply system.

Therefore, at the preliminary stage of detector calibration, we precalibrate the SiPMs. In this way, the response nonlinearity and the T-dependence of SiPM parameters are largely corrected for. The precalibration procedure is devised so that the relevant SiPM parameters can be promptly estimated using the statistics of a single data file.

At the next stage, all detector and veto system channels are fully calibrated using cosmic muons. Since the statistics of cosmic particles is limited, this requires analyzing a large volume of data equivalent to several hours of data accumulation. On this time scale, variations in detector characteristics can be neglected, since the temperature drifts of SiPM channels are
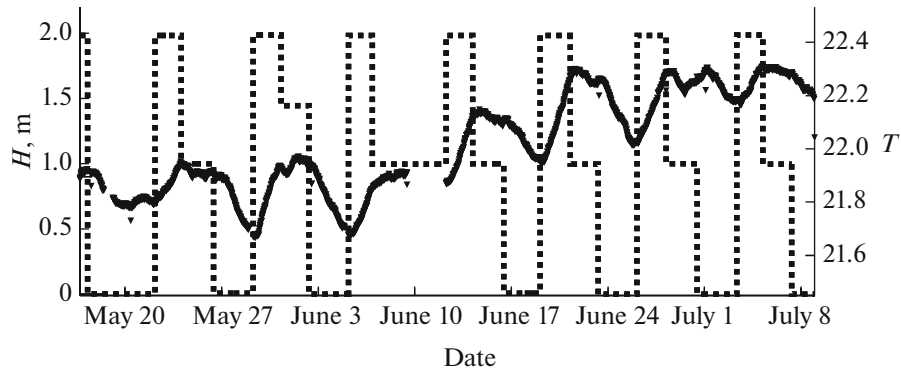
Fig. 4. Time dependence of the mean temperature of readout planes compared with that of the detector position with respect to the reactor core (dashed line) over the period from May 17 through July 9 of 2017.

largely compensated for at the precalibration stage, whereas the PMT characteristics are relatively stable (see Section 7 below).

The techniques for precalibrating the SiPMs and calibrating the detector as a whole are elaborated in Sections 5 and 6, respectively.

5. PRECALIBRATION OF SILICON PHOTOMULTIPLIERS

The silicon photomultiplier [2] is a compact matrix of pixels with $p-n$ junctions operating in the mode of restricted Geiger discharge. A photon hitting the photosensitive area can, with a certain probability, generate a free charge carrier (an electron or a hole), which then reaches the multiplication area and induces an avalanche in one of the $p-n$ junctions. The pixel operates in the binary mode, i.e., the magnitude of its signal is independent of the number of free carriers inducing the discharge. Since the total SiPM response is a net signal of all pixels, it is proportional to the total number of incident photons given a low exposure. The SiPM linearity is maintained as soon as the firing of a $p-n$ junction by two or more electron–hole pairs occurs with a negligibly small probability. With

Fig. 5. SiPM saturation curve.

increasing density of the light flux, this condition is violated and the so-called saturation effect sets in. The SiPM saturation curve is described by the dependence
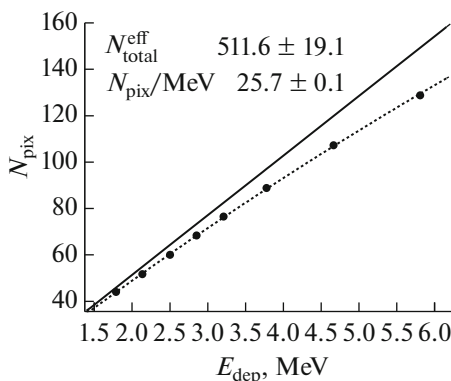
$$N_{\mathrm{pix}} = N_{\mathrm{total}} \times \left[1 - e^{-N_{\mathrm{c}}/N_{\mathrm{total}}} \right], \qquad (1)$$

where N_{total} denotes the total number of constituent pixels, N_{c} is the mean number of free charge carriers capable of causing Geiger discharges, and N_{pix} is the initial number of thereby induced avalanches. We have $N_{\mathrm{c}} = N_{\mathrm{ph}} \times PDE$, where N_{ph} is the number of photons hitting the sensitive area and PDE is the photon detection efficiency. In a sense, quantity N_{c} is analogous to the number of photoelectrons emitted by the photocathode of an ordinary vacuum PMT.

In the case of the DANSS experiment, a SiPM square-shaped sensitive area is connected to a cylindrical optical fiber of a smaller radius. Since not all pixels are illuminated under these conditions, in Eq. (1) one has to substitute the effective number of pixels $N_{\mathrm{total}}^{\mathrm{eff}}$, which is somewhat smaller than their total number N_{total}.

The parameter $N_{\mathrm{total}}^{\mathrm{eff}}$ is measured experimentally using the tracks of minimum ionizing particles (MIPs) reconstructed in the detector. The true value of energy deposition in the detector, E_{dep}, is inferred from the length of track section within one cell. The most probable value of the MIP specific energy loss is obtained via a detailed simulation of the detector response based on the GEANT4 code [3]. The number of avalanches N_{pix} is inferred from the net signal I using the values of SiPM parameters obtained at the precalibration stage as discussed below.

The experimentally obtained saturation curve is shown in Fig. 5, where N_{pix} is plotted as a function of E_{dep}. The fitting curve shown by the dashed line is a functional form involving two parameters: $N_{\mathrm{total}}^{\mathrm{eff}}$ and the slope of the N_{pix} linear dependence on E_{dep} in the region of small deposited energies. The latter linear dependence, shown by the solid line in Fig. 5, corre-
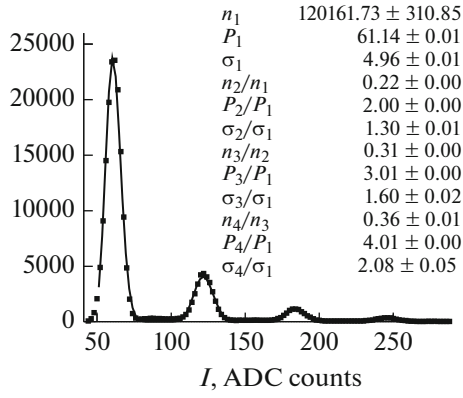
Fig. 6. Example of the SiPM noise spectrum fitted to a sum of Gaussians (solid curve).

Fig. 7. P_1 distributions plotted prior to and upon the SiPM hardware calibration (asterisks and solid line, respectively).

sponds to the number of fired pixels expected in the absence of saturation. In inverse β-decay, the range of positron energy extends up to 8 MeV, where the saturation effect plays an important role. The thus-measured effective number of pixels, $N_{total}^{eff} = 512 \pm 19$, proved to be significantly less than their total number of $N_{total} = 667$.

Yet another SiPM characteristic is the degree of optical crosstalk between the pixels. Namely, secondary photons emitted in a Geiger discharge can induce avalanches in the $p-n$ junctions of neighboring pixels. The optical crosstalk is quantified as the mean number of fired pixel junctions per initial avalanche, referred to as the Geiger-discharge multiplication factor X.

Thus, in order to derive the number of originally fired pixels from the net signal I and then obtain the N_c value using the inverted saturation curve, one needs the following input parameters: (a) the SiPM gain K in the form of the one-pixel-avalanche contribution to the integral signal and (b) the multiplication factor X, whereby the number of original Geiger discharges can be inferred from that of detected avalanches. The precalibration of silicon photomultipliers is aimed at determining the values of these two parameters for each SiPM channel by analyzing its dark noise spectrum.

With no external illumination, a SiPM with supplied voltage generates small amplitude pulses of dark current arising from spontaneous Geiger avalanches in pixel $p-n$ junctions. The frequency of these pulses usually amounts to tens of kHz, depending on the applied voltage and external temperature. A dark noise pulse is indistinguishable from that induced by an incident photon. Since the original discharge generates secondary ones through the optical crosstalk between neighboring pixels, the dark-noise spectrum is a sequence of equidistant peaks with decreasing amplitudes.

A typical dark noise spectrum of an individual SiPM of the DANSS detector is shown in Fig. 6. The peak positions P_1, P_2, P_3, etc., are proportional to the
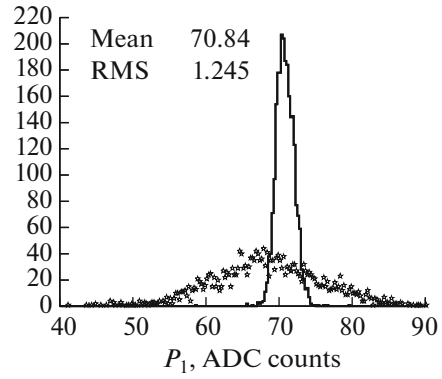
corresponding numbers of fired pixels. The value of P_1 defines the SiPM gain K. The multiplication factor X can be determined by comparing the event statistics in different peaks, since these are proportional to the avalanche probability in the corresponding number of photodetector pixels. In this, we rely on the analytical model of optical crosstalk developed in [4].

For precalibrating the SiPMs, the DAQ system of the DANSS experiment features the so-called calibration trigger, which is activated by a nonzero signal from an arbitrary SiPM channel. Of the events selected by this trigger, only a small fraction is preserved because of the high frequency of the dark noise. The decimation factor is selected so that the statistics of noise spectra logged on a file together with the data are sufficient to precalibrate each SiPM channel.

At the start of the DANSS experiment, the above method was employed to produce the set of individual SiPM operating voltages, i.e., for hardware calibration of the detector. The initial SiPM voltages were crudely adjusted so as to approximately equalize the currents in all channels. Then, two data samples were collected under two different voltages V_1 and V_2. In this way the parameters of the linear $P_1(V)$ dependences were obtained and then used for setting the nominal voltages.

The working point was selected as $P_1^{nom} = 70$ ADC counts. The P_1 distributions for nominal voltages prior to and upon hardware calibration are shown in Fig. 7 (asterisks and solid line, respectively). Through the hardware calibration, the P_1 spread was reduced from 10.6 down to 1.8%, which was sufficient to start a massive accumulation of physical data.

The stability of the parameters K and X from May 17 through July 10 of 2017 is illustrated by bottom curves in Figs. 8a and 9a, respectively. In either case, plotted vs the date is the relative parameter variation with respect to the benchmark value averaged over all SiPM channels (in percent). Here and in what follows, the benchmark sample is selected as the data file
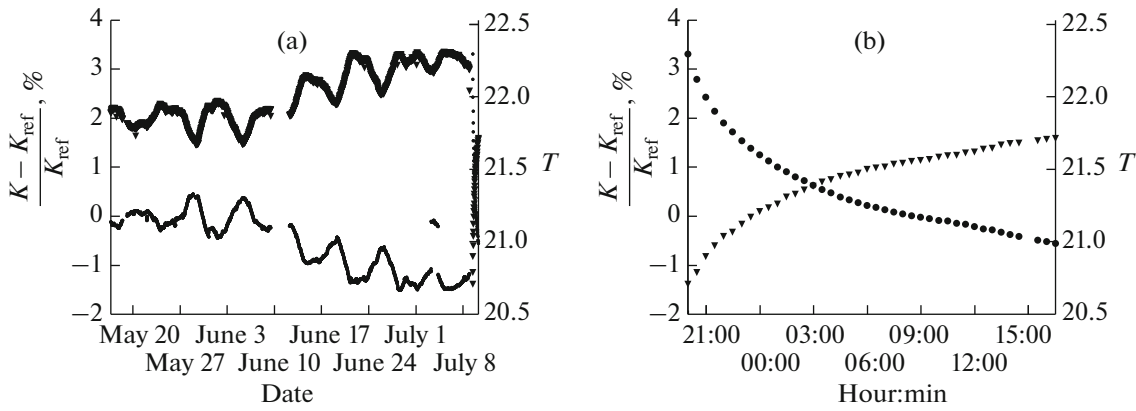
Fig. 8. Left-hand panel: time dependence of the mean variation of SiPM gain K (bottom curve) compared with that of the mean temperature (top curve) over the period from May 17 through July 10, 2017. (a) After the electricity breakdown, the stabilization of K (triangles) and (b) the mean temperature (dots) over a zoomed time scale.
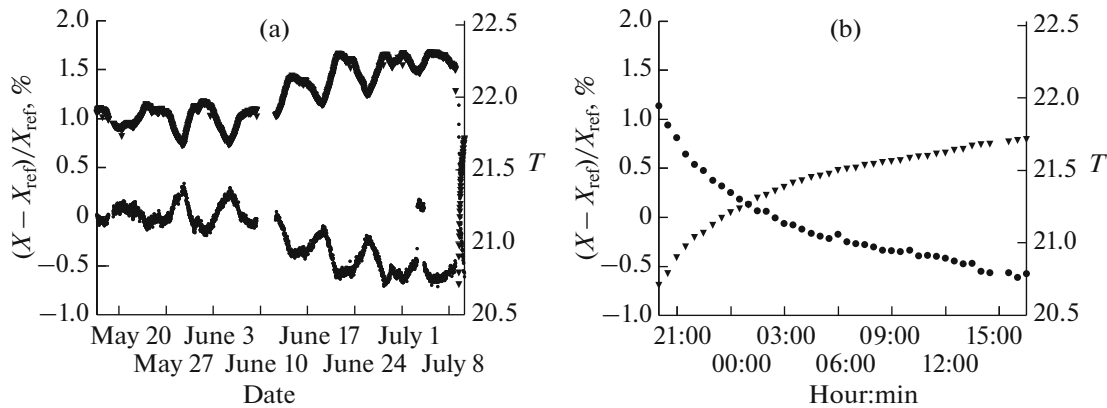
Fig. 9. Left-hand panel: time dependence of the mean variation of the Geiger-discharge multiplication factor X (bottom curve) compared with that of the mean temperature (top curve) over the period from May 17 through July 10, 2017. (a) After the electricity breakdown, the stabilization of X (triangles) and (b) the mean temperature (dots) over a zoomed time scale.

20 289 collected at noon of May 19, 2017 amid a period of relatively stable temperatures when the detector position was not changed for several days (see Fig. 4). The time dependence of the temperature T throughout the same period is depicted by the upper curves in Figs. 8a and 9a. The K and X variations are seen to be correlated with those of the mean temperature. In these figures, the time interval is extended by 1.5 days compared to Fig. 4 so as to include the first hours of detector operation after a nine-hour emergency shutdown which resulted in a significant cooling of the readout planes. With a zoomed timescale, the K and X stabilization processes upon switching on the SiPM voltages are shown in Figs. 8b and 9b, respectively.

Note that, for both parameters, the data points for July 3−4, 2017, lie far above the expected positions. This had been caused by a unqiue disruption of output voltage settings in several SiPM power supply modules which was then automatically corrected by the monitoring software.

6. OVERALL CALIBRATION WITH PHYSICAL SIGNALS

For a precalibrated SiPM, the N_c value corrected for the saturation effect is derived from the net signal I. The quantity N_c is interrelated with the energy in physical units by analyzing the spectrum of energies deposited by cosmic muons. For the vacuum photomultipliers, including those of the veto system, such spectra are produced directly using the net signals I. Only the particles with trajectories orthogonal to scintillator slabs are selected for the calibration. This is aimed at minimizing the particle path within a cell, module, or veto counter. The latter is particularly important for PMTs, for which even such signals lie in the upper one-third of the dynamic range of readout ADCs.
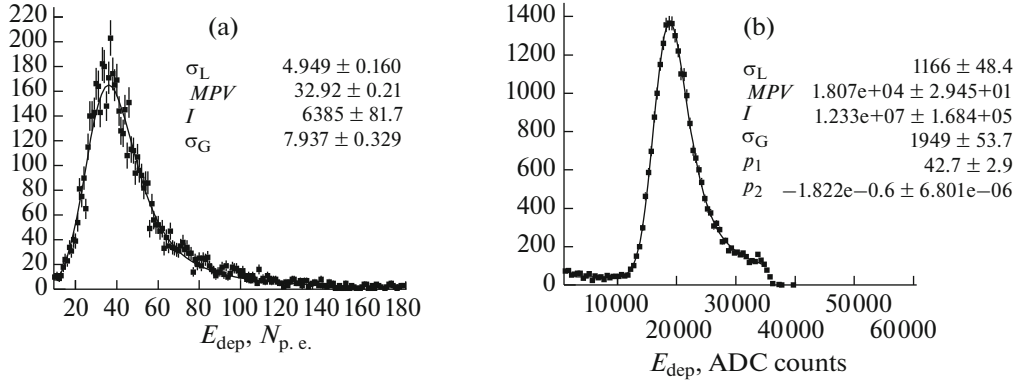
Fig. 10. Examples of the distributions of MIP energy deposition for a SiPM channel (a) and for a PMT channel (b). The fits of these distributions are depicted by solid lines. For the SiPM channel, the fitting function is a convolution of Landau and Gaussian distributions with respective widths σ_L and σ_G, the most probable value MPV, and integral I. For the PMT channel, the fitting function also features an exponential term of $p_1 \times e^{p_2 \times E_{dep}}$ for describing the background pedestal.

For the SiPM and PMT channels, individual spectra of the energies deposited by muons are exemplified in Figs. 10a and 10b, respectively. In either case, a distinct peak is a signal from minimum ionizing particles. For PMTs, the steep downfall of the spectrum tail corresponds to large signals falling beyond the upper boundary of the ADC dynamic range. Such PMT signals are excluded from the analysis.

The MIP peak is fitted to a convolution of Landau and Gauss distributions. Of these, the former describes particle losses in the scintillator and the latter describes the probability for photons hitting the sensitive area to generate free charge carriers or photoelectrons. In the PMT case, the MIP peak sits on top of a background pedestal. The latter is accounted for by adding an exponential term to the fitting function.

The most probable value of the MIP energy loss, MPV_{MIP}, is selected as a calibration parameter. This is compared with the predicted value derived through a detailed simulation of the detector response. The simulated response to cosmic muons is processed with the same code as that used for calibration of the detector. For a normally incident MIP, the most probable value of energy loss amounts to 1.57 MeV for a cell; 18.5 MeV for a module; and 7−12 MeV for a veto counter, depending on its particular geometry.

The statistics of cosmic particles required for one cycle of MIP-based calibration of all detector channels is equivalent to at least 30 data files. This corresponds to 13−15 h of standard running. Since temperature effects are largely compensated for at the stage of SiPM precalibration (see Section 7), such a cycle frequency is more than sufficient for reliable calibration of the detector and for monitoring the stability of its response.

7. READOUT CHAIN STABILITY AND COMPENSATION FOR TEMPERATURE EFFECTS

The stability of the detector readout chain is tested using the data collected from May 17 through July 10, 2017. The mean relative variation of MPV_{MIP} for vertical MIPs with respect to the nominal value is selected as a criterium of stable operation. The data are averaged over all photodetector channels of the same type and processed using two different methods as described below.

(1) A single set of individual SiPM parameters K and X obtained from the benchmark file 20289 is used for testing SiPM stability. The processing results are shown in Fig. 11, where the MPV_{MIP} mean relative variation is depicted by dots. This is plotted vs. the mean date of data collection for groups of 30 data files used for obtaining a set of the energy deposition spectra for cosmic muons. Also shown is the time dependence of the mean temperature T (triangles). This distribution features the T value for the median file of each group; therefore, in Fig. 11 the T variation appears to be less pronounced than in the previous figures dealing with individual files. On the whole, we may conclude that for SiPMs the mean MPV_{MIP} variation reaches almost 5% even under the conditions of a long period of continuous detector operation.

(2) Towards estimating the degree to which the temperature effects are compensated by precalibrating the SiPMs, we employ standard data processing extracting the K and X parameters of each SiPM independently for each data file. The results shown in Fig. 12 demonstrate that the MPV_{MIP} residual variations do not exceed 1.7%. These can be attributed to variations in the photon detection efficiency (PDE), which involves a T-dependent factor for the Geiger-discharge probability.
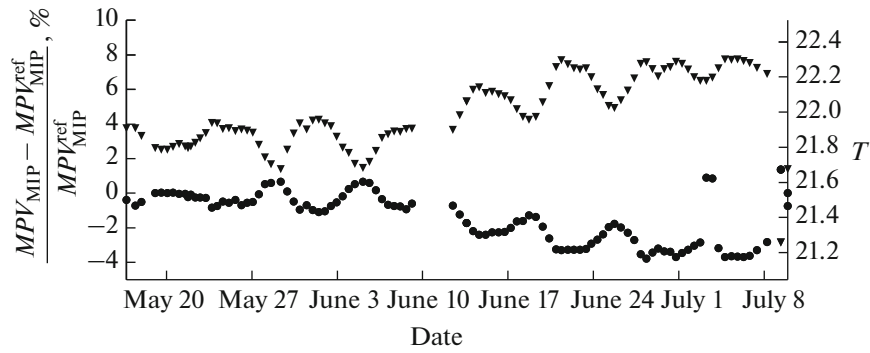
Fig. 11. Readout chain stability with no file-by-file corrections for the SiPM channels (dots) compared with the time dependence of mean temperature (triangles).
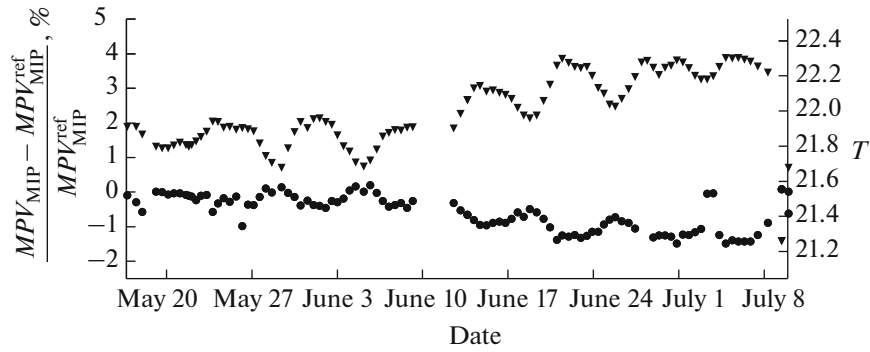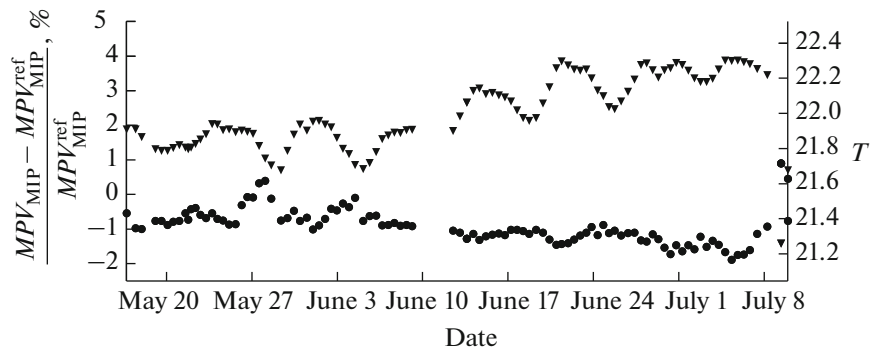

Fig. 12. Readout chain stability upon applying the file-by-file corrections for the SiPM channels (dots) compared with the time dependence of mean temperature (triangles).

The PMT mean stability is illustrated in Fig. 13. For routine mode of data taking, the MPV_{MIP} mean variation is seen to stay within ±1%. Prior to physics analysis of the collected data, a MIP-based calibration is performed whereby residual variations of the readout chain parameters are compensated for in due time.

8. MEASURING THE LIGHT YIELD AND ITS LONGITUDINAL DEPENDENCE

The precalibration of SiPMs helps extract the light yield Y as an important cell parameter directly from the collected data. The light yield is defined as the mean number of photons emitted by the scintillator

Fig. 13. Readout chain stability for the PMT channels (dots) compared with the time dependence of mean temperature (triangles).
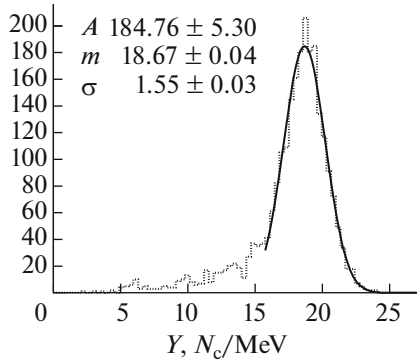
Fig. 14. Light yields of scintillator strips measured with SiPMs.

upon absorbing unit energy. Because in practice one usually deals with a detector channel formed by a scintillator strip, its light-collection system, and a photodetector, quantity Y is calculated in terms of the number of photoelectrons (for PMTs) or free charge carriers (for SiPMs).

In the DANSS experiment, knowledge of light yields is mainly required for consistently simulating the detector operation and for estimating the contribution of statistical fluctuations in photodetectors to the energy resolution of the detector.

In the process of calibration with the physical signal, the Y value for each channel is obtained as $Y = N_c^{MIP}/MPV_{MIP}$, where MPV_{MIP} is the most probable value of the vertical MIP energy deposition in MeV and N_c^{MIP} is the corresponding number of free charge carriers.

The Y distribution for all SiPM channels of the detector is shown in Fig. 14. This is plotted with the statistics of nearly 400 data files logged over a period of stable temperature of readout planes, which amounted to 21.8° on average. The cell-by-cell spread of the light

yield largely arises from different qualities of the optical contact between the wavelength shifting fiber and the SiPM sensitive area. For a few SiPM channels, the light yield was degraded by disrupting their optical contacts during the assembly of one of the lower sections of the detector. All other cells have uniform light yields with a mean number of 18.67 free charge carriers per MeV and a Y distribution with an rms width of 8%.

For the PMT channels, the light yield is estimated through illumination with short pulses from an external light-emitting diode (LED). Thereby, several data samples for different values of the light signal amplitude were written on disk. The LED voltage was varied so as to cover the full dynamic range of readout ADCs.

Given a sufficient amount of light and a fixed LED voltage, the spectrum of the LED-induced PMT signal is a Gaussian with a mean value of I_{LED} and a width of σ_{LED}. The number of photoelectrons $N_{p.e}$ is statistically determined as

$$N_{p.e} = \left(I_{LED}/\sigma_{LED}\right)^2. \qquad (2)$$

A typical I_{LED}-dependence of $N_{p.e}$ for a PMT channel is shown in Fig. 15a, where I_{LED} values have been recalculated to those of the equivalent deposited energy. For each PMT channel, this dependence is produced and then fitted to a linear form whose slope finally gives the value of Y. A thus-obtained Y distribution for all DANSS modules is shown in Fig. 15b. The light yield has a mean value of 14 ph.e./MeV and is distributed with an rms width of 10%.

In estimating $N_{p.e}$ with Eq. (2), one implicitly assumes that width σ_{LED} is fully determined by fluctuations of the number of photoelectrons emitted by the PMT photocathode. This is not completely true, since the width also picks certain contributions from fluctuations of the multiplication factors of PMT dynodes, particularly of the first one. In the DANSS conditions, this contribution is estimated as 20−30% and can be removed by, e.g., analyzing the processes of one-pho-
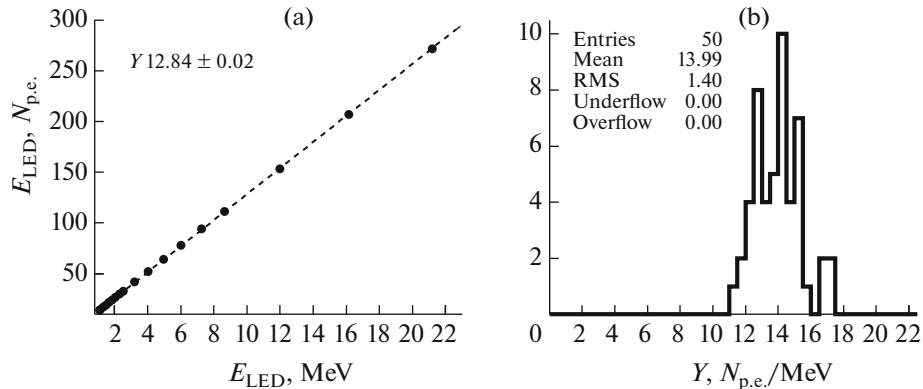
Fig. 15. (a) A typical dependence of the number of photoelectrons on the mean LED signal. (b) Light yields of detector modules measured with PMTs.

$A1$	0.0323 ± 0.0162
$c1$	-0.0515 ± 0.0092
$A2$	0.9686 ± 0.0181
$c2$	-0.0015 ± 0.0004
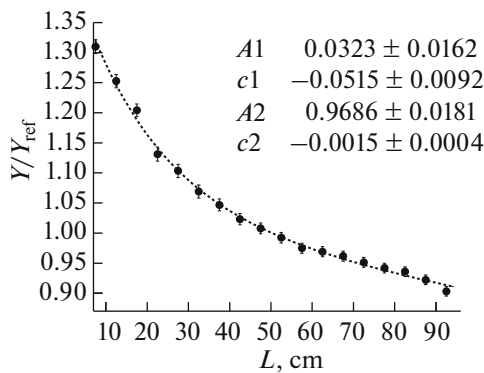
Fig. 16. Light yield dependence on the hit longitudinal position on the scintillator strip. The dashed curve is the fit to a sum of two exponentials.

ton electron emission (such measurements are scheduled for the future). However, it should be emphasized that knowledge of the PMT total resolution is essential for developing a valid simulation procedure.

The light is significantly attenuated when propagating through the wavelength shifting fiber. Specific attenuation is the same for all detector channels, since it is fully determined by the fiber properties. As a result, light yield Y depends on the longitudinal distance between the interaction point and the sensitive area of the photodetector.

For a large fraction of detected events, the particle hits at least two neighboring mutually orthogonal strips so that the longitudinal variation of the light yield can be corrected for by reconstructing the hit positions in scintillator slabs. The attenuation curve is measured using the tracks of cosmic muons, since these traverse multiple strips and are accurately reconstructed in space. The measured attenuation curve is shown in Fig. 16, where L is the hit−SiPM distance and the plotted quantity is MPV_{MIP} as a function of L divided by that for a reference distance equal to the

strip half-length. The observed L-dependence of the light yield is fitted to a sum of two exponentials (dashed line in Fig. 16). The hits close to the strip edge faces have been rejected in order to exclude any boundary effects. Over the full strip length, the attenuation reaches 30% (with respect to the light yield for the minimum L value).

9. CONCLUSIONS

The DANSS neutrino spectrometer was commissioned in March 2016 and thoroughly tested from April through September of the same year. The experiment has been accumulating physical data for over a year. From the start of physical running, the variations in detector characteristics largely determined by those of the external temperature are promptly corrected for using the developed calibration procedures. The computer model of the detector aimed at simulating its operation benefited from measuring the light yields of scintillator strips. The simulation plays a decisive role in estimating the efficiency of antineutrino detection and in optimizing the algorithms for reconstructing the events of inverse β-decay. Our preliminary measurements of reactor-antineutrino spectra and our constraints on the sterile neutrino mixing parameters have been reported at a number of scientific conferences and published in [5].

The DANSS detector has been monitoring the reactor power P since October 2016. For the fourth block of the Kalinin nuclear power plant, the instantaneous P value as a function of time is shown in Fig. 17 (dotted curve) from October 2016 through May 2017 (these data have been provided by the staff of the nuclear power plant). The DANSS measurements of this quantity based on the detected inverse-β-decay events are depicted by the data points. The data points are normalized to the curve by the 12 consecutive points corresponding to the time period of November
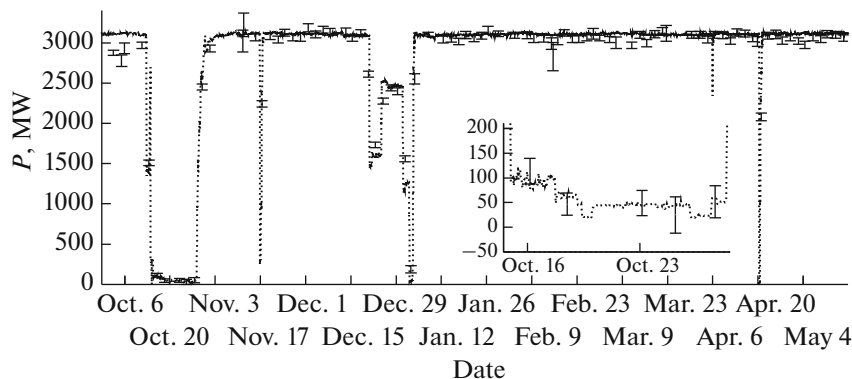
Fig. 17. Time dependence of the nominal reactor power (dotted curve) compared with that of the DANSS signal (data points) over the period from October 2016 through May 2017. The time interval corresponding to a partial shutdown of the reactor in the second half of October 2016 is shown in the inset with a zoomed time scale.

and December of 2016. The DANSS data collected at different distances r from the reactor core have been renormalized to the smallest distance. With a zoomed time scale, the reactor shutdown period in the second half of October 2016 is shown by the inset in Fig. 17. DANSS is seen to adequately monitor the reactor operation even at low values of generated power. This indicates that the DANSS experimental procedure is robust.

ACKNOWLEDGMENTS

REFERENCES

1. I. Alekseev et al. (DANSS Collab.), "DANSS: detector of the reactor anti neutrino based on solid scintillator," J. Instrum. **11**, 11011 (2016).

2. S. Klemin, Yu. Kuznetsov, L. Filatov, P. Buzhan, B. Dolgoshein, A. Il'in, and E. Popova, "Silicon photoelectronic multiplier. New opportunity," Elektron.: Nauka, Tekhnol. Biznes, No. 8, 80−86(2007).

3. S. Agostinelli et al., "Geant4 a simulation toolkit," Nucl. Instrum. Methods Phys. Res., Sect. A **506**, 250−303 (2003).

4. L. Gallego, J. Rosado, F. Blanco, and F. Arqueros, "Modeling crosstalk in silicon photomultipliers," J. Instrum. **8**, 05010 (2013).

5. I. Alekseev et al. (DANSS Collab.), "Detector of the reactor antineutrino based on solid-state plastic scintillator (DANSS). Status and first results," J. Phys.: Conf. Ser. **798**, 012152 (2017).

Translated by A. Asratyan